

## Near-Range Large Field-of-View Three-Dimensional Photon-Counting Imaging with a Single-Pixel Si-Avalanche Photodiode \*

Guang-Yue Shen(申光跃)<sup>1</sup>, Tian-Xiang Zheng(郑天翔)<sup>1</sup>, Bing-Cheng Du(杜秉乘)<sup>1</sup>, Yang Lv(吕阳)<sup>1</sup>,  
E Wu(武愕)<sup>1</sup>, Zhao-Hui Li(李召辉)<sup>1\*\*</sup>, Guang Wu(吴光)<sup>1,2\*\*</sup>

<sup>1</sup>State Key Laboratory of Precision Spectroscopy, East China Normal University, Shanghai 200062

<sup>2</sup>Collaborative Innovation Center of Extreme Optics, Shanxi University, Taiyuan, Shanxi 030006

(Received 6 August 2018)

*Large field-of-view (FoV) three-dimensional (3D) photon-counting imaging is demonstrated with a single-pixel single-photon detector based on a Geiger-mode Si-avalanche photodiode. By removing the collecting lens (CL) before the detector, the FoV is expanded to  $\pm 10^\circ$ . Thanks to the high detection efficiency, the signal-to-noise ratio of the imaging system is as high as 7.8 dB even without the CL when the average output laser pulse energy is about 0.45 pJ/pulse for imaging the targets at a distance of 5 m. A 3D image overlaid with the reflectivity data is obtained according to the photon-counting time-of-flight measurement and the return photon intensity.*

PACS: 42.68.Wt, 42.30.Wb, 42.79.Pw, 85.60.Dw

DOI: 10.1088/0256-307X/35/11/114204

Light detection and ranging (LIDAR) systems based on the time-correlated single-photon counting (TCSPC) technique have been widely used in remote sensing applications including terrain mapping,<sup>[1–4]</sup> underwater imaging<sup>[5,6]</sup> and autonomous vehicle vision monitoring.<sup>[7–10]</sup> Most of the LIDAR systems can be classified into the co-axial<sup>[11–16]</sup> and the bi-axial ones<sup>[17–21]</sup> according to the relative positions of the emitter and the receiver. In the co-axial LIDAR system, since the emitter channel and the receiver channel share a number of optical components and the collected return photons are focused statically on the detector when the laser beam scans the target, single-pixel detectors of small-active area are usually used. With a low-noise single-pixel single-photon detector, depth imaging at range of 4.5 km using a pulsed laser with output energy of 15 pJ/pulse has been achieved.<sup>[22]</sup> However, the field-of-view (FoV) of this co-axial LIDAR system was merely  $1.6^\circ$ ,<sup>[6]</sup> which severely limited its application. In the bi-axial LIDAR system, the focus spot of the return photons on the detector will move when the direction of the emitting laser or the distance of the target changes. Therefore, array detectors with large active area are favored in such systems, such as multi-pixel photon counters (MPPCs) and complementary metal-oxide semiconductor (CMOS) image sensors.<sup>[23–27]</sup> On the one hand, the FoV of the LIDAR system can be much expanded using large-active-area array detectors. On the other hand, the high background noise due to the large active area of the MPPC and the CMOS image sensor would have a pernicious influence on the reconstruction of the targets in the LIDAR system. In addition, the cost of such array detectors is quite expensive due to the difficulties in fabrication of highly

integrated numerous pixels of balanced noise level and detection efficiency. Therefore, it will become a focus of research interest to develop the large-FoV three-dimensional (3D) laser imaging system with a single-pixel detector in real applications.

In this Letter, we demonstrate a large-FoV 3D photon-counting imaging system in a bi-axial configuration with a single-pixel Si-avalanche photodiode (Si-APD) single-photon detector (SPD) of a small active area as the receiver. The collecting lens (CL) in front of the detector is removed to eliminate the influence of the moving focal spot. By this means, the FoV of the system is expanded to  $\pm 10^\circ$ . Thanks to the high detection efficiency, without the CL, we could still obtain a high signal-to-noise ratio to extract the return photon signals from the noise for even fairly low reflected photon flux. A large-FoV 3D photon-counting image is demonstrated with target scene at 5 m in the lab. Moreover, combined with the intensity of the return photons, the reflectivity data are overlaid on the 3D image.

The near-range large-FoV 3D photon-counting imaging system is schematically shown in Fig. 1. The optical transceiver system was operated in the bi-axial mode. The laser source (LD852VFP, Nanjing K-Ray Opto-Electronics, China) used in the experiment was a pulsed diode laser with a multi-mode fiber pigtail emitting at 850 nm. The average output power of the laser was  $4.5 \mu\text{W}$  at a repetition frequency of 10 MHz. The laser output energy was calculated to be about 0.45 pJ/pulse. The pulse width of the laser was approximately 1.3 ns. The laser beam at the output of the multi-mode fiber was expanded by an optical collimator. The diameter of the laser beam was 5 mm with divergence angle of 0.7 mrad. Then the

\*Supported by the National Natural Science Foundation of China under Grant Nos 11774095, 11722431 and 11621404, the Shanghai Basic Research Project under Grant No 18JC1412200, the National Key R&D Program of China under Grant No 2016YFB0400904, the Program of Introducing Talents of Discipline to Universities under Grant No B12024, and the Shanghai International Cooperation Project under Grant No 16520710600.

\*\*Corresponding author. Email: zhkli@lps.ecnu.edu.cn; gwu@phy.ecnu.edu.cn

© 2018 Chinese Physical Society and IOP Publishing Ltd

laser beam was directed by a pair of galvanometer mirrors (GMs, S-9210M, Sunny Technology, China). The sizes of the GM were about  $10\text{ mm}\times 19\text{ mm}$  and  $16\text{ mm}\times 20\text{ mm}$ , respectively. The GMs were driven by a data acquisition card (DAQ, USB-6343, National Instruments, USA) to scan the targets in both horizontal and vertical directions. The scanning resolution of the GMs was set at  $0.17^\circ/\text{step}$  in both directions. An interference bandpass filter (850FS10-25, Andover Corporation, USA) was placed in front of the Si-APD. The return photons were detected directly by the single-pixel Si-APD (SAP500, Laser Components, Germany). The diameter of the detector's active area was about  $500\text{ }\mu\text{m}$ . The Si-APD was operated in Geiger-mode with a bias voltage at  $122.7\text{ V}$ . The detection efficiency of the SPD at the wavelength of  $850\text{ nm}$  was about  $60\%$  with a dark count rate of  $200\text{ count/s}$  when the operation temperature was kept at  $-35^\circ\text{C}$ .

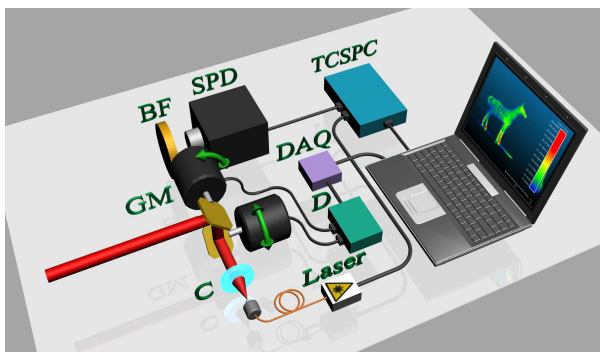


**Fig. 1.** Schematic diagram of the near-range large-FoV three-dimensional photon-counting imaging system. Laser: pulsed laser emitting at  $850\text{ nm}$  with a repetition rate of  $10\text{ MHz}$  and a pulse duration of  $1.3\text{ ns}$ . GMs: galvanometer mirrors with sizes of  $10\text{ mm}\times 19\text{ mm}$  and  $16\text{ mm}\times 20\text{ mm}$ , respectively. D: servo driver of the GMs. BF: interference bandpass filter at  $850\text{ nm}$  with a bandwidth of  $10\text{ nm}$ . DAQ: data acquisition device. SPD: single-photon detector based on Si-APD. TCSPC: time-correlated single-photon counter. C: collimator.

In the normal configuration, a lens is usually inserted in front of the detector to collect the return photons. The selection of the lens should obey several rules. First, the aperture of the lens should be large to collect enough return photons for detection. Secondly, the focus length of the lens should quite short to produce a small focus spot on the active area of the SPD as well as a small movement of the focus spot when the laser scans. However, the focus spot of the lens will still move away from the small active area of the detector, limiting the FoV of the LIDAR system.

Firstly, we verified the FoV in the normal configuration by putting a convex lens in front of the detector as the collecting lens. The focus length of the lens was  $25.4\text{ mm}$  and the diameter was  $25.4\text{ mm}$ . A white board was placed at  $5\text{ m}$  as the target. The photon-counting rate from the SPD was monitored while the laser scanned. For analysis, a temporal gate was applied on the output of the SPD in the data processing.

The width of the gate was set at  $1.5\text{ ns}$ , which was the same as the temporal resolution of the LIDAR system. Only the photon counting within the gate was recorded, including the signal photons and the background noise photons. Figure 2(a) shows the photon-counting rates as a function of the scanning angle of the laser beam with the CL in the horizontal and the vertical directions, respectively. The FoVs were only  $\pm 0.5^\circ$  in both directions. The photon-counting rate dropped quickly when the laser-scanning angle was beyond the FoV since the focus spot of the return photons was out of the active area of the detector.

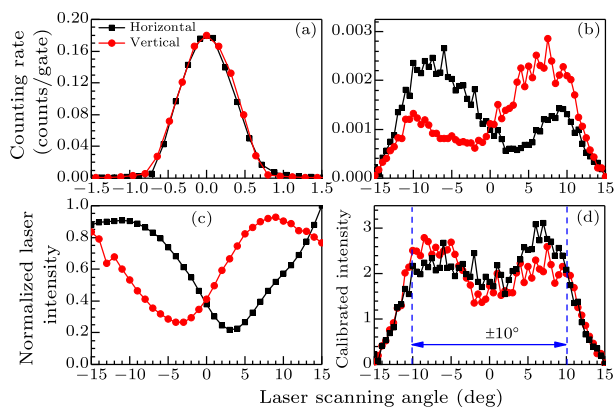


**Fig. 2.** (a) FoV of the photon-counting imaging system with the CL. (b) FoV of the photon-counting imaging system without the CL. (c) Laser intensity as a function of the scanning angle. (d) Calibrated FoV without the CL.

Then, we removed the collecting lens in front of the detector. The imaging system was easier to align more stably since the SPD was exposed directly to the return photon flux. The counting rate of the return photons dropped from  $0.18\text{ count/gate}$  to  $0.99 \times 10^{-3}\text{ count/gate}$  when the laser aimed at the same spot in the center of the target. Meanwhile, the background noise of the system also decreased from  $0.38 \times 10^{-3}\text{ count/gate}$  to  $0.11 \times 10^{-3}\text{ count/gate}$ . The signal-to-noise ratio dropped from  $132.7\text{ dB}$  to  $7.8\text{ dB}$  according to the equations in Ref. [28]. The FoVs of the system were found to be  $\pm 10^\circ$  in both horizontal and vertical directions as shown in Fig. 2(b). By removing the collecting lens in front of the detector, the FoV of the system was much expanded at the expense of decreasing the detected return photon signals. Thanks to the high detection efficiency, the return photon signals could still be identified from the background noise at a distance of  $5\text{ m}$ . In principle, the FoV of the SPD is determined by the size of the active area and the configuration of the Si-APD, which is calculated to be about  $\pm 58^\circ$ . However, the FoV was limited by the bandpass filter in this system. Since the narrow-linewidth interference bandpass filter was employed in the system to extract the return photons from the background noise, the accepting angle of the filter is small. If a combination of absorption filters can be used in the system, the FoV could be further extended. [22]

Ideally, the response curve of the detector should be flat and symmetric in both horizontal and vertical directions as the laser scans since the active area of the APD is round. However, there was a dip in the detector's response as a function of the laser scanning angle as shown in the measured FoV curves in Fig. 2(b). We found that the unbalanced response was caused by the imperfection of the GMs. The laser power measured after the GMs varied with the scanning angle in Fig. 2(c). It also shows that the detector's response was proportional to the reflected photon intensity, which makes it possible to reconstruct a surface reflectivity profile of the target according to the detected photon intensity. We normalized the intensity response of the system within the FoV according to the laser output power after the GMs at different scanning angles as shown in Fig. 2(d). We found that with the correction, the detector's response was almost flat within the FoV ( $\pm 10^\circ$ ). In this way, the surface reflectivity carried by the detected return photon intensity could be read out correctly.

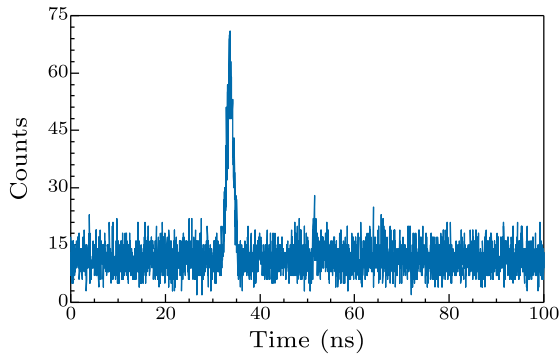


**Fig. 3.** ToF measurement without the CL. SPD counting rate:  $98.3 \times 10^3$  count/s. Integration time: 0.4 s. Temporal resolution of the TCSPC: 32 ps. Target distance: 5 m.

We verified the depth resolution of the near-range photon-counting imaging system. The output of the SPD was connected to the STOP port of the time-correlated single-photon counter (TCSPC, Hydraharp 400, PicoQuant, Germany). The START port of the TCSPC was connected by the laser synchronous signal for the time-of-flight measurement. The temporal resolution of the TCSPC was set at 32 ps and the acquisition time was set at 0.4 s. Taking into account the pulse duration of the laser source, the time jitter of the detector and the TCSPC time bin width, the temporal resolution of the LIDAR system was calculated according to

$$\Delta t = \sqrt{t_L^2 + t_{\text{SYNC}}^2 + t_D^2 + t_{\text{TCSPC}}^2}, \quad (1)$$

where  $t_L$  is the pulse duration of the laser source (1.3 ns),  $t_{\text{SYNC}}$  is the time jitter of the synchronous signal ( $< 10$  ps),  $t_D$  is the time jitter of the detector ( $\sim 800$  ps), and  $t_{\text{TCSPC}}$  is the time bin width of the TCSPC (32 ps). Figure 3 shows the histogram of time of flight (ToF) of the detected photons without the

CL at around 5 m. The measured temporal resolution was 1.5 ns, in good agreement with the theoretic prediction. The remove of the CL did not change the temporal resolution of the imaging system. Therefore, the depth resolution of the 3D photon-counting imaging system was 22.5 cm. The ToF measurement was repeated ten times and we determined the depth measurement precision of 25.7 mm by the standard division of the peak positions in the ToF measurements.

We demonstrated the near-range large-FoV 3D photon-counting imaging in the corridor of the lab at a distance of 5 m. The target scene was comprised of a model of a horse and a carton as shown in Fig. 4(a). The horse was about 1.6 m tall and placed 1.2 m from the wall. It was made of white plastic. Black tapes were glued to the horse body to form a pattern of ECNU. The carton was  $0.5 \times 0.5 \times 0.5$  m<sup>3</sup> and was placed close to the wall. A pattern of LPS was glued on the front surface of the carton. The scanned area was mapped by  $100 \times 164$  pixel corresponding to a pixel-to-pixel interval of approximately 14.8 mm in both horizontal and vertical directions at the target plane. The scanning angle of the laser covered  $\pm 14^\circ$  in horizontal direction and  $\pm 8.5^\circ$  in vertical direction in the experiment. The beam diameter at the target was around 8.5 mm, meaning that there was no overlap between adjacent pixels for each scan position. At each point, the ToF was measured and recorded together with the GM positions. In this way, a 3D image could be built.

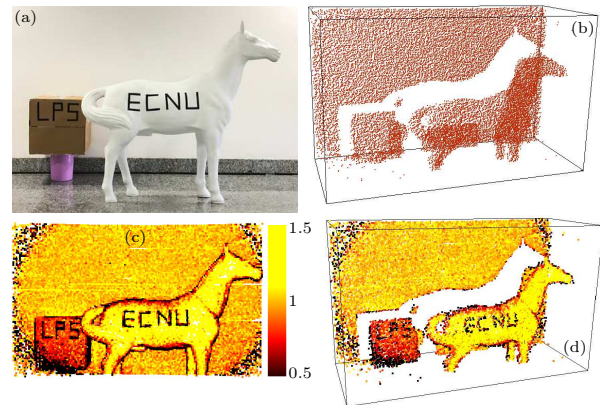


**Fig. 4.** (a) Photograph of the target scene. (b) The  $100 \times 164$  pixel depth profile of the target scene. (c) Reflectivity reconstruction of the target scene according to the return photon intensity. (d) The 3D reconstruction of the target scene overlaid with reflectivity data.

The lights in the laboratory corridor were turned off, the data were acquired with a background noise counting rate of around  $94 \times 10^3$  count/s. On account of a display screen in the lobby of the lab, which emitted high background light, the background noise is large. The background noise could be decreased using a narrower band-pass filter. In the experiment, an interference filter of 10-nm bandwidth was used. Decreasing the bandwidth will limit the FoV. Next, we used the absorption filter to solve this problem. Be-

cause of the low reflectivity of the pattern on the horse, the acquisition time of per-pixel was set as 0.4 s. Using the TCSPC method, the ToF and the count of the signal peak were recorded pixel by pixel. The distance  $D$  was calculated by

$$D = \frac{cT}{2}, \quad (2)$$

where  $T$  is the ToF measured in the experiment, and  $c$  is the speed of light in vacuum. Combining the scanning angle in the horizontal and the vertical directions at each pixel, the data could be obtained according to

$$X = D \sin \theta \cos \varphi, \quad (3)$$

$$Y = D \sin \theta \sin \varphi, \quad (4)$$

$$Z = D \cos \theta, \quad (5)$$

where  $\theta$  and  $\varphi$  denote scanning angles of the laser in horizontal and vertical directions, respectively, corresponding to the position in polar coordinate system, and  $X$ ,  $Y$  and  $Z$  are the position in Cartesian coordinates system. Figure 4(b) shows the depth profile of the target scene. The surface of the horse can be clearly recognized. In addition, the size of the carton indicates the correctness of the image. Since the scanning angle was slightly larger than the FoV, we can see that the corners of the image were blurred due to less detected signal photons out of the FoV.

Figure 4(c) shows the detected photon intensity image of the scene in two dimensions without the distance information. The image was corrected according to the laser power after the GMs. The color bar scales the detected photon intensity from low to high with dark red to bright yellow. The horse is yellow due to the high reflectivity of the white plastic. The carton is light red due to the low reflectivity of the brown cardboard. The black patterns on the horse body and the carton are in dark red since few photons were reflected from there. It is clear to observe the sympatric FoV in this image due to the round shape of the Si-APD's active area. Then, we rendered the 3D image in Fig. 4(b) with the detected photon intensity data in Fig. 4(c). Figure 4(d) shows the 3D photon-counting image overlaid with reflectivity data. The black patterns on the back of the horse and the carton can be identified to stick to the surface.

In conclusion, we have constructed a large-FoV 3D photon-counting imaging system in bi-axial configuration using a single-pixel Si-APD single-photon detector of small active area as the receiver. By removing the CL in front of the detector, the influence of the moving focal spot is eliminated and the FoV of the system is expanded to  $\pm 10^\circ$ . Due to the high detection efficiency of the single-photon detector used in the system, a high signal-to-noise ratio is obtained to extract the return photon signals from the noise for even fairly low return photon level. Combined with the intensities of the return photons, a large-FoV three-dimensional imaging overlaid with reflectivity data for

the targets with a stand-off distance of 5 m is demonstrated. The system shows robustness and simplicity due to the reducing of optic components. This near-range large-FoV 3D photon-counting imaging system may be applied to the autonomous vehicle vision monitor systems in the near future where compact short-distance large-FoV 3D imaging is favored.

## References

- [1] Podgórski J, Pęćlicki M and Kinnard C 2018 *Cold Reg. Sci. Technol.* **151** 288
- [2] Schwarz B 2010 *Nat. Photon.* **4** 429
- [3] Swatantran A, Tang H, Barrett T, DeCola P and Dubayah R 2016 *Sci. Rep.* **6** 28277
- [4] Tarolli P 2014 *Geomorphology* **216** 295
- [5] Halimi A, Maccarone A, McCarthy A, McLaughlin S and Buller G S 2017 *IEEE Trans. Comput. Imag.* **3** 472
- [6] Maccarone A, McCarthy A, Ren X, Warburton R E, Wallace A M, Moffat J, Petillot Y and Buller G S 2015 *Opt. Express* **23** 33911
- [7] Pierzchała M, Giguère P and Astrup R 2018 *Comput. Electron. Agr.* **145** 217
- [8] Liang W, Zhang Y and Wang J 2017 *IFAC PapersOnLine* **50** 276
- [9] Wang H, Wang B, Liu B, Meng X and Yang G 2017 *Robot. Auton. Syst.* **88** 71
- [10] Broggi A, Grisleri P and Zani P 2013 *Int. IEEE Conf. Intelligent Transportation Syst.* p 887
- [11] McCarthy A, Collins R J, Krichel N J, Fernández V, Wallace A M and Buller G S 2009 *Appl. Opt.* **48** 6241
- [12] Henriksson M, Larsson H, Grönwall C and Tolt G 2016 *Opt. Eng.* **56** 031204
- [13] Pawlikowska A M, Halimi A, Lamb R A and Buller G S 2017 *Opt. Express* **25** 11919
- [14] Tobin R, Halimi A, McCarthy A, Ren X, McEwan K, Stephen M and Buller G S 2017 *Opt. Eng.* **57** 031303
- [15] Chen S, Liu D, Zhang W, You L, He Y, Zhang W, Yang X, Wu G, Ren M, Zeng H, Wang Z, Xie X and Jiang M 2013 *Appl. Opt.* **52** 3241
- [16] Zhou H, He Y, You L, Chen S, Zhang W, Wu J, Wang Z and Xie X 2015 *Opt. Express* **23** 14603
- [17] Cui Z, Tian Z, Zhang Y, Bi Z and Fu S 2018 *Optik* **157** 768
- [18] Sun M J, Edgar M P, Gibson G M, Sun B, Radwell N, Lamb R and Padgett M J 2016 *Nat. Commun.* **7** 12010
- [19] Li Z, Wu E, Pang C, Du B, Tao Y, Peng H, Zeng H and Wu G 2017 *Opt. Express* **25** 10189
- [20] Peng H, Wang Y R, Meng W D, Yan P Q, Li Z H, Li C, Pan H F and Wu G 2018 *Optoelectron. Lett.* **14** 0129
- [21] Xu L, Zhang Y, Zhang Y, Wu L, Yang C, Yang X, Zhang Z and Zhao Y 2017 *Appl. Opt.* **56** 3059
- [22] McCarthy A, Ren X, Della Frera A, Gemmell N R, Krichel N J, Scarcella C, Ruggeri A, Tosi A and Buller G S 2013 *Opt. Express* **21** 22098
- [23] Niclass C, Soga M, Matsubara H, Kato S and Kagami M 2013 *IEEE J. Solid-State Circuits* **48** 559
- [24] Ren X, Connolly P W R, Halimi A, Altmann Y, McLaughlin S, Gyongy I, Henderson R K and Buller G S 2018 *Opt. Express* **26** 5541
- [25] Krstajic N, Pol, S, Levitt J, Walker R, Erdogan A, Ameer-Beg S and Henderson R K 2015 *Opt. Lett.* **40** 4305
- [26] Jahromi S, Jansson J P and Kostamovaara J 2016 *Opt. Express* **24** 21619
- [27] Gyongy I, Calder N, Davies A, Dutton N A W, Dalgarno P, Duncan R, Rickman C and Henderson R K 2018 *IEEE Trans. Electron Devices* **65** 547
- [28] Sara P, Gerald S B, Jason M S, Andrew M W and Sergio C 2000 *Meas. Sci. Technol.* **11** 712